Angular-Momentum-Resolved Rydberg State Population of Argon Ions in Strong Laser Fields

Zhigang Zheng[1,2†], Di Wang[1,2†], Mingyue Wang[1,2], Li Wang[1,2], Xu Sun[1,2], Jing Zhao[1,2,3], Zhihui Lv[1,2,3], Xiaowei Wang[1,2,3*], and Zengxiu Zhao[1,2,3*]

[1]*Department of Physics, National University of Defense Technology, Changsha 410073, China*
[2]*Hunan Key Laboratory of Extreme Matter and Applications, National University of Defense Technology, Changsha 410073, China*
[3]*Hunan Research Center of the Basic Discipline for Physical States, National University of Defense Technology, Changsha 410073, China*

(Received 24 February 2025; accepted manuscript online 25 March 2025)

This letter demonstrates an experimental approach to measuring the angular-momentum-resolved population of excited states in laser-produced argon ions. By measuring the spectra of free induction decay emissions corresponding to the resonant transitions between Rydberg states, the relative population of the Rydberg states is obtained with known Einstein A-coefficients. This study deepens the mechanistic understanding of coherent dynamics in laser-driven ionic excited states, and establishes experimental benchmarks essential for validating and refining advanced quantum kinetic models in strong-field physics.

DOI: 10.1088/0256-307X/42/5/053702 CSTR: 32039.14.0256-307X.42.5.053702

Strong-field ionization and excitation, as fundamental processes in laser-matter interactions, have been extensively studied both theoretically and experimentally.[1–6] Among these processes, the population of ionic excited states after strong-field ionization is a critical yet complex phenomenon, involving an intricate interplay between multi-electron correlations, electronic coherence, and subsequent free induction decay (FID).[7–12] Understanding the population distribution of these states is essential for unraveling non-equilibrium plasma dynamics and optimizing applications ranging from high-harmonic generation (HHG) to laser-induced breakdown spectroscopy (LIBS).[13–17]

Recent advances in attosecond metrology have significantly improved our understanding of strong-field ionization dynamics.[12,18–21] However, few studies have focused on the post-ionization dynamics,[22–24] particularly the population distribution of ionic excited states induced by femtosecond laser pulses. Previous studies[25,26] typically assumed local thermal equilibrium (LTE), where excited-state populations follow the Boltzmann distribution. The transition probabilities can be estimated by measuring the spontaneous emission spectrum, which corresponds only to the transition probability and the population of the upper level and results in fluorescence. However, this framework fails in strong field regimes, where attosecond-scale ionization processes drive systems far from equilibrium. For neutral atoms, Zimmermann 0demonstrated a field-ionization depletion method to measure the distribution of helium (He) Rydberg state populations by controlling external electric fields.[27] Although effective for neutral species, this method cannot directly access ionic excited states because of their higher binding energies in electric fields, and is not capable of resolving excited states with different angular momentum. Traditional ionic diagnostics, such as photoelectron spectroscopy and ion mass spectrometry, primarily resolve charge-state distributions or dynamics of direct ionization yields,[28,29] but neglect metastable excited states. On the other hand, the FID radiation, which is emitted during the field-free transitions between coherent superposition states induced by strong laser fields, encodes the population information of Rydberg states.[22,30–32] However, the quantitative determination of relative populations across multiple excited states remains unexplored.

In this study, the FID spectra of argon (Ar) atoms exposed to intense femtosecond laser fields were measured. The spectra reveal distinct emission signatures of excited states for both neutral atoms and singly ionized ions (Ar^+). By systematically analyzing spectral features and comparing transitions sharing a common lower energy level in Ar^+, we obtained quantitative population distributions across multiple upper energy levels. This approach enabled the determination of relative state populations induced by strong-field excitation, as well as the refinement of selected Einstein A-coefficients. These findings advance the understanding of coherent dynamics in laser-driven ionic systems and establish empirical benchmarks for modeling multielectron correlation effects under extreme electromagnetic fields.

†These authors contributed equally to this work.
*Corresponding author. Email: xiaowei.wang@nudt.edu.cn; zhaozengxiu@nudt.edu.cn
© 2025 Chinese Physical Society and IOP Publishing Ltd. All rights, including for text and data mining, AI training, and similar technologies, are reserved.

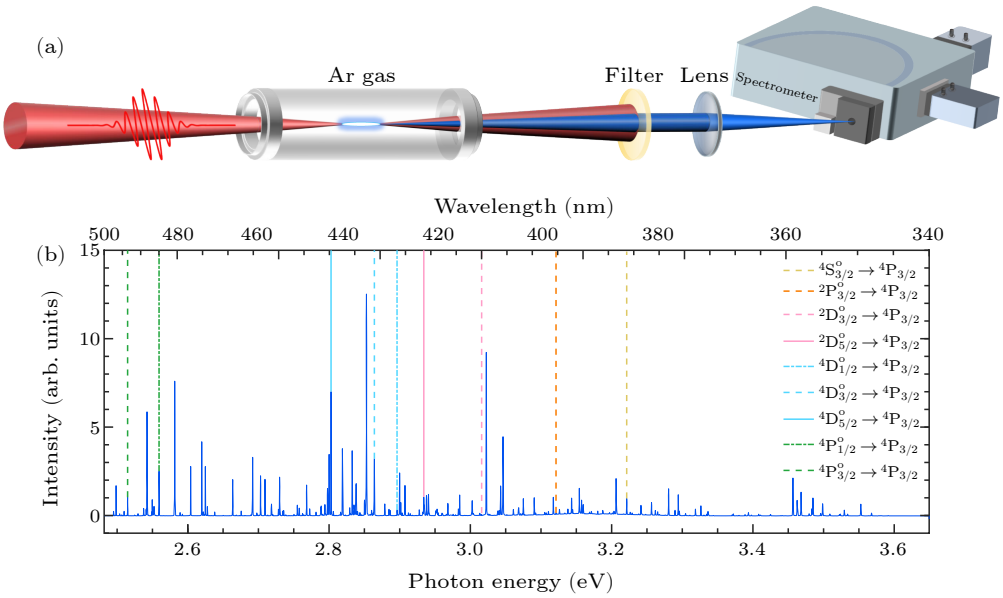

Fig. 1. (a) Schematic of the experimental setup. (b) Spectrum recorded using the spectrometer. Some transitions are marked at the corresponding positions, omitting the common 3p electron configuration $3s^2\,3p^4(^3P)$ for the simplification of expression. The corresponding lower levels and upper levels of transitions are labeled in the legend.

A schematic of the experimental setup is depicted in Fig. 1(a). The 25 fs, 4.2 mJ near infrared (NIR) driving laser pulses were delivered by a 10-pass Ti:sapphire amplifier (Femtopower Pro HE) with a repetition rate of 1 kHz. The pulses were focused by a plano-convex lens ($f = 250$ mm) onto Ar atoms contained in a gas cell with a backing pressure of 5 mbar. The peak laser intensity was adjusted to be around 1.5 PW/cm^2, so that substantial Rydberg states could be populated via multi-photon excitation or frustrated tunneling ionization. After the laser field vanished, all the excited states decayed by transitioning to lower energy states, giving rise to line emissions known as FID. The FID was separated from the residual NIR beam by a spectral filter, and then coupled to a spectrometer (Andor SR500i) with a resolution of 0.03 nm, which measured the spectral lines between 340 nm and 500 nm. Note that the driving laser intensity should be kept moderate. If the laser intensity is too high, the spectral broadening may extend below 500 nm, thereby hindering spectral detection. However, if the laser intensity is too low, the decreasing population of the excited state can weaken the spectral intensity.

Figure 1(b) shows a measured FID spectrum, exhibiting abundant spectral lines each corresponding to a certain transition path. By comparing with the energy levels of Ar Rydberg states reported in previous studies [33–38] and the NIST atomic database, [39] the observed spectral lines are unambiguously assigned to FID processes between the excited states of neutral Ar atoms and Ar^+ ions. Most of the spectral lines originate predominantly from Ar^+, some of which are labeled as vertical lines. The line width of each FID emission is measured to be around 6×10^{-4} eV, due to the high-resolution spectrometer. While most of the spectral lines are detached, some of the emissions still overlap with each other, since the energy levels are so close. In addition, the emissions around 3.1 eV have constant backgrounds due to second harmonic generation of the fundamental beam in nonlinear interactions. To obtain the spectral intensity for each emission line, different procedures are conducted for the three following cases:

- Resolved lines. For spectrally isolated lines, the intensity is determined by integrating the total signal over the entire line profile $I_i = \int S(\varepsilon)\,\mathrm{d}\varepsilon$, where $S(\varepsilon)$ denotes the measured spectral intensity at photon energy of ε.
- Overlapping lines. For spectrally overlapping transitions with discernible peaks, as shown in Fig. 2(a), the line profiles can be fitted by multiple Lorentzian profiles:

$$I_{\text{total}} = \sum_i \frac{I_i}{1 + \left(\frac{\varepsilon - \varepsilon_i}{\Gamma_i}\right)^2}, \tag{1}$$

  where I_i represents the peak amplitude of the i-th line, ε_i denotes the corresponding photon energy, and Γ_i is the spectral width. In the fitting process, the initial values for the peak intensities of different spectral lines are determined by the experimental spectral data. Finally, the spectral intensity can be integrated with the corresponding fitted spectral lines.
- Indistinguishable spectral lines with constant background. Some of the emission lines are too close to each other, making them indistinguishable by the spectrometer, as shown in Fig. 2(b). Although it appears to be a well-resolved separate emission line, there are two different transition lines according to reported energy levels. Furthermore, the spectral baseline does not drop to zero, indicating the existence of a constant background. The background is actually the second harmonic of the

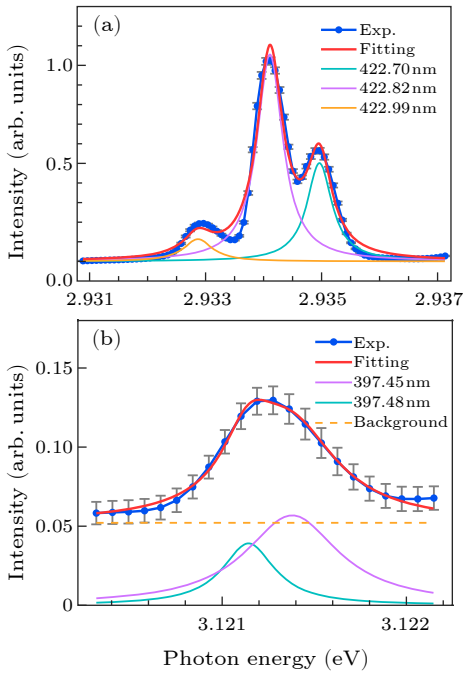

Fig. 2. Two typical cases of spectral overlap. (a) Overlap between the spectral lines with distinguishable peaks. (b) Complete overlap of the spectral lines with non-zero baseline, which is the second harmonic generated by the nonlinear process of the laser in Ar.

fundamental NIR field. The two spectral profiles can still be extracted following the same fitting procedure wit Eq. (1), but with an additional offset to include the constant background. In the fitting process, the initial values for the peak intensities of different spectral lines are given according to the relative intensity (RI) ratios provided by NIST database. The spectral intensities of each line can thus be obtained by integrating the fitted profile.

This systematic treatment of complex spectra significantly reduces measurement inaccuracies arising from spectral overlap.

Due to the relatively low pressure of Ar in the experiments, the de-excitation caused by collisions between electrons and ions is neglectable. The spectral intensity of the FID emission during the transition between the $|\psi_m\rangle$ and $|\psi_i\rangle$ states should satisfy

$$I_{mi} \propto |\langle c_i\psi_i|\boldsymbol{r}|c_m\psi_m\rangle|^2, \tag{2}$$

where c_i and c_m are the corresponding wave function amplitudes of $|\psi_i\rangle$ and $|\psi_m\rangle$, respectively. Meanwhile, the Einstein coefficient A_{mi} can be described by

$$A_{mi} \propto |\langle\psi_i|\boldsymbol{r}|\psi_m\rangle|^2. \tag{3}$$

For two spectral lines sharing the same lower level i, e.g., I_{mi} and I_{ni}, the relative population ratio can be obtained according to Eqs. (2) and Eq. (3) as follows:

$$\frac{N_m}{N_n} = \frac{|c_m|^2}{|c_n|^2} = \frac{I_{mi}A_{ni}}{I_{ni}A_{mi}} \tag{4}$$

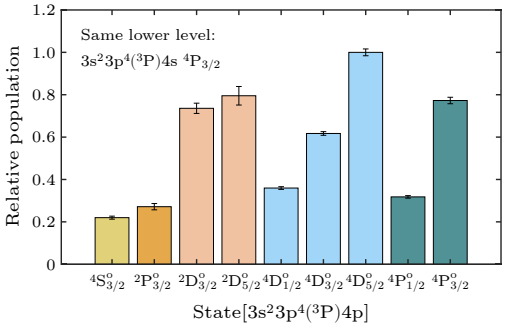

Fig. 3. The relative populations of different Ar^+ excited states. The lower level is indicated at the top left, and the x-axis displays the specific terms and total angular momentum (denoted by the subscript) of the different upper levels.

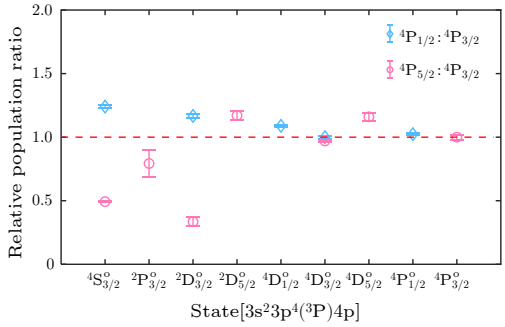

Fig. 4. The relative population ratios of different groups with shared upper levels. The red dashed line represents the reference line with a ratio of 1. In the data processing, the upper level [$3s^2\,3p^4(^3P)4p\,^4P^o_{3/2}$ and $3s^2\,3p^4\ (^3P)4p\,^4D^o_{3/2}$, respectively], corresponding to the A_{ki} with the highest accuracy, are used as the reference. The pink and blue data points represent the ratios of the relative populations obtained from two different groups based on distinct lower levels. The groups are labeled in the legend.

For the spectrum shown in Fig. 1(b), we extract the relative population of a group of energy levels ($^4S^o_{3/2}$, $^2P^o_{3/2}$, $^2D^o_{3/2}$, $^2D^o_{5/2}$, $^4D^o_{1/2}$, $^4D^o_{3/2}$, $^4D^o_{5/2}$, $^4P^o_{1/2}$, and $^4P^o_{3/2}$) sharing the same electron configuration $3s^2\,3p^4(^3P)4p$ by looking into the transitions from these states to a common lower level $3s^2\,3p^4(^3P)4s\,^4P_{3/2}$. The relative populations among these upper levels are calculated using Eq. (4), as shown in Fig. 3. The population for different states with different orbital angular momentum L and total angular momentum J is quite different, which may serve as an experimental benchmark for developing strong field excitation models.

For a certain energy level, there are lots of transition channels, and every transition emission can be used to calculate the population, providing a way to cross check the extraction. Focusing on the same states in Fig. 3, we choose two additional destination energy levels with $3s^2\,3p^4(^3P)4s\,^4P_{1/2}$ and $3s^2\,3p^4(^3P)4s\,^4P_{5/2}$ for population extraction with the same protocol. The results are normalized to the earlier-obtained population with $3s^2\,3p^4(^3P)4s\,^4P_{3/2}$ being the destination energy level, and the relative population ratios are shown in Fig. 4. The blue data points represent ratios of retrieved population with the lower levels of $3s^2\,3p^4\ (^3P)4s\,^4P_{1/2}$ and $3s^2\,3p^4(^3P)4s\,^4P_{3/2}$,

Table 1. A summary of the transition parameters and derived A_{ki} values with uncertainties. The accuracy reported by NIST [39] is indicated in parentheses when the uncertainty data are not available in Ref. [33]. The letter 'A' means the highest accuracy with a deviation within 5%, while 'E' indicates the lowest accuracy with a deviation exceeding 50%.

Lower level $3s^2\,3p^4(^3P)4s$	Upper level $3s^2\,3p^4(^3P)4p$	Wavelength (nm)	RI [37]	A_{ki} [33] ($10^6\,s^{-1}$)	Exp. intensity (arb. units)	Population	Derived A_{ki} ($10^6\,s^{-1}$)
$^4P_{1/2}$	$^2S^o_{1/2}$	392.24	2	$0.3 \pm 22\%$	$0.246 \pm 3.70\%$	$1.68 \pm 3.70\%$	
	$^4S^o_{3/2}$	392.86	191	$24.4 \pm 13\%$	$5.24 \pm 3.13\%$	$0.442 \pm 3.13\%$	
	$^2P^o_{3/2}$	405.77	1	0.02(E)	0	0	
	$^2P^o_{1/2}$	414.74	2	0.018(E)	0	0	
	$^2D^o_{3/2}$	420.20	59	$2.1 \pm 20\%$	$1.42 \pm 0.466\%$	$1.39 \pm 0.466\%$	$2.45 \pm 15.9\%$
	$^4D^o_{1/2}$	437.97	550	$100.4 \pm 4\%$	$31.0 \pm 2.00\%$	$0.635 \pm 2.00\%$	
	$^4D^o_{3/2}$	443.02	661	$56.9 \pm 4\%$	$27.7 \pm 1.53\%$	$1.00 \pm 1.53\%$	
	$^4P^o_{1/2}$	497.22	100	$9.7 \pm 7\%$	$2.49 \pm 1.68\%$	$0.527 \pm 1.68\%$	
$^4P_{3/2}$	$^2S^o_{1/2}$	384.46	6	0.3(E)	0	0	
	$^4S^o_{3/2}$	385.06	263	$38.7 \pm 12\%$	$5.81 \pm 3.24\%$	$0.220 \pm 3.24\%$	
	$^2P^o_{3/2}$	397.45	50	$2 \pm 50\%$	$0.371 \pm 5.47\%$	$0.272 \pm 5.47\%$	
	$^2P^o_{1/2}$	406.05		0.0032(C)	0	0	
	$^2D^o_{3/2}$	411.28	513	$1.1 \pm 14\%$	$0.553 \pm 3.29\%$	$0.736 \pm 3.29\%$	
	$^2D^o_{5/2}$	422.82	331	$13.1 \pm 3\%$	$7.12 \pm 5.51\%$	$0.795 \pm 5.51\%$	
	$^4D^o_{1/2}$	428.29	68	$13.2 \pm 9\%$	$3.24 \pm 1.78\%$	$0.360 \pm 1.78\%$	$12.1 \pm 8.28\%$
	$^4D^o_{3/2}$	433.12	603	$57.4 \pm 5\%$	$24.2 \pm 1.41\%$	$0.617 \pm 1.41\%$	
	$^4D^o_{5/2}$	442.60	1514	$81.7 \pm 5\%$	$55.8 \pm 1.61\%$	$1.00 \pm 1.61\%$	
	$^4P^o_{1/2}$	484.78	832	$84.9 \pm 9\%$	$18.4 \pm 1.88\%$	$0.318 \pm 1.88\%$	
	$^4P^o_{3/2}$	493.32	251	$14.4 \pm 5\%$	$7.60 \pm 1.97\%$	$0.773 \pm 1.97\%$	
$^4P_{5/2}$	$^4S^o_{3/2}$	372.93	234	$48.0 \pm 10\%$	$3.64 \pm 2.66\%$	$0.140 \pm 2.66\%$	
	$^2P^o_{3/2}$	384.54	32	$1.6 \pm 22\%$	$0.241 \pm 47.4\%$	$0.279 \pm 47.4\%$	
	$^2D^o_{3/2}$	397.48	15	$0.9 \pm 50\%$	$0.155 \pm 11.7\%$	$0.319 \pm 11.7\%$	$0.301 \pm 19.6\%$
	$^2D^o_{5/2}$	408.24	76	$2.9 \pm 7\%$	$1.89 \pm 1.90\%$	$1.20 \pm 1.90\%$	
	$^4D^o_{3/2}$	417.84	13	$1.2 \pm 18\%$	$0.502 \pm 1.01\%$	$0.775 \pm 1.01\%$	$1.16 \pm 8.34\%$
	$^4D^o_{5/2}$	426.65	288	$16.4 \pm 11\%$	$13.3 \pm 2.29\%$	$1.50 \pm 2.29\%$	$19.0 \pm 8.62\%$
	$^4D^o_{7/2}$	434.81	1995	$117.1 \pm 4\%$	$100 \pm 1.59\%$	$1.58 \pm 1.59\%$	
	$^4P^o_{3/2}$	473.59	1000	$58.0 \pm 3\%$	$31.4 \pm 1.91\%$	$1.00 \pm 1.91\%$	
	$^4P^o_{5/2}$	480.60	1820	$78.0 \pm 4\%$	$57.2 \pm 2.07\%$	$1.36 \pm 2.07\%$	

while the pink data points correspond to ratios with $3s^2\,3p^4(^3P)4s\,^4P_{5/2}$ and $3s^2\,3p^4\ (^3P)4s\,^4P_{3/2}$. In principle, the relative population will always be the same, i.e., the ratio should be 1, regardless of which transition path is utilized. Although most ratios are close to 1, the ratios of $^4S^o_{3/2}$, $^2P^o_{3/2}$, and $^2D^o_{3/2}$ states are far from 1, implying inconsistent population extraction from different transition channels.

It is important to note that the error bars in Fig. 4 reflect statistical uncertainties from repeated measurements, but do not account for systematic errors arising from A_{ki} uncertainties. Previous studies [33,39] show that A_{ki} is less accurate for the transitions to $^4S^o_{3/2}$, $^2P^o_{3/2}$, and $^2D^o_{3/2}$ states compared to the other destination states. This in turn provides a way to correct inaccurate A_{ki} values. According to Eq. (4), the Einstein coefficient A_{mi} for the transition from the upper level m: $3s^2\,3p^4(^3P)4p\,^2D^o_{3/2}$ to lower level i: $3s^2\,3p^4(^3P)4s\,^4P_{5/2}$ transition deduced from another more accurate Einstein coefficient A_{ni}:

$$A_{mi} = \frac{N_n \times I_{mi}}{N_m \times I_{ni}} A_{ni}. \tag{5}$$

The A_{mi} derived from Eq. (5) may offer improved accuracy compared to current reference data. [33,39] Specifically, if another upper level n: $3s^2\,3p^4(^3P)4p\,^4P^o_{3/2}$ and lower level j: $3s^2\,3p^4(^3P)4s\,^4P_{3/2}$ are chosen for Eq. (5), considering both the accumulation of the uncertainty in Einstein coefficients and the uncertainty in experimental data, the final result is $A_{mi} = 3.01 \times 10^5\,s^{-1} \pm 19.6\%$. This result shows a smaller uncertainty than that in Refs. [33,39]. All the numerical data used in these calculations, including the transitions, wavelengths, RI and A_{ki} values from previous studies, [33,37,39] spectral intensities, relative populations of upper levels, and derived A_{ki} values with uncertainties, are summarized in Table 1.

In summary, we experimentally measured the FID spectra of Ar^+ after excitation and ionization driven by strong laser fields. Through systematic analysis of these spectra, we determined the relative populations of various Ar^+ excited states. Cross-validation among different transition channels confirmed the methodological rigor and reproducibility of our analytical approach. Notably, our findings reveal discrepancies with existing atomic databases, prompting us to put forth updated reference values for key Einstein A-coefficients with reduced uncertainty margins compared to previous studies. This work provides critical insights into the ultrafast ionic dynamics following strong-field interactions while delivering a valu-

able experimental framework for benchmarking advanced theoretical models in strong-field physics.

Acknowledgements. This work is supported by the National Natural Science Foundation of China (Grant Nos. 12234020, 12474281, 12450403, and 12274461), and the Science and Technology Innovation Program of Hunan Province (Grant No. 2022RC1193).

References

[1] Corkum P B 1993 *Phys. Rev. Lett.* **71** 1994
[2] Tong X M, Zhao Z X, and Lin C D 2002 *Phys. Rev. A* **66** 033402
[3] Nubbemeyer T, Gorling K, Saenz A, Eichmann U, and Sandner W 2008 *Phys. Rev. Lett.* **101** 233001
[4] Paul P M, Toma E S, Breger P, Mullot G, Augé F, Balcou P, Muller H G, and Agostini P 2001 *Science* **292** 1689
[5] Goulielmakis E, Loh Z H, Wirth A, Santra R, Rohringer N, Yakovlev V S, Zherebtsov S, Pfeifer T, Azzeer A M, Kling M F, Leone S R, and Krausz F 2010 *Nature* **466** 739
[6] Lei H, Yao J, Zhao J, Xie H, Zhang F, Zhang H, Zhang N, Li G, Zhang Q, Wang X, Yang Y, Yuan L, Cheng Y, and Zhao Z 2022 *Nat. Commun.* **13** 4080
[7] Brewer R G and Shoemaker R L 1972 *Phys. Rev. A* **6** 2001
[8] Zhou Y, Huang C, Liao Q, and Lu P 2012 *Phys. Rev. Lett.* **109** 053004
[9] Wang Y, Yu S, Sun R, Kang H, Xu S, Lai X, Quan W, and Liu X 2024 *Phys. Rev. Lett.* **132** 223202
[10] Zhang X, Lu Q, Zhu Y, Zhao J, Danylo R, Xu L, Lei M, Jiang H, Wu C, Zhang Z, Houard A, Tikhonchuk V, Mysyrowicz A, Gong Q, Zhuang S, Zhao Z, and Liu Y 2024 *Ultrafast Sci.* **4** 0051
[11] Chen Y, Peng S, Fu Z, Qiu L, Fan G, Liu Y, Wu S, Xie X, and Tao Z 2024 *Commun. Phys.* **7** 98
[12] Wang L, Bai G, Wang X, Zhao J, Gao C, Wang J, Xiao F, Tao W, Song P, Qiu Q, Liu J, and Zhao Z 2024 *Nat. Commun.* **15** 2705
[13] Lewenstein M, Balcou P, Ivanov M Y, L'Huillier A, and Corkum P B 1994 *Phys. Rev. A* **49** 2117
[14] Zhang D W, Lü Z H, Meng C, Du X Y, Zhou Z Y, Zhao Z X, and Yuan J M 2012 *Phys. Rev. Lett.* **109** 243002
[15] Wang L, Xiao F, Song P, Tao W, Sun X, Wang J, Zheng Z, Zhao J, Wang X, and Zhao Z 2023 *Chin. Phys. Lett.* **40** 114203
[16] Labutin T A, Lednev V N, Ilyin A A, and Popov A M 2016 *J. Anal. At. Spectrom.* **31** 90
[17] Zhao S, Zhao Y, Dai Y, Liu Z, Zha H, and Gao X 2024 *Front. Phys.* **19** 62500
[18] Sainadh U S, Xu H, Wang X, Atia-Tul-Noor A, Wallace W C, Douguet N, Bray A, Ivanov I, Bartschat K, Kheifets A, Sang R T, and Litvinyuk I V 2019 *Nature* **568** 75
[19] Li S, Driver T, Rosenberger P *et al.* 2022 *Science* **375** 285
[20] Wang X, Xiao F, Wang J, Wang L, Zhang B, Liu J, Zhao J, and Zhao Z 2024 *Ultrafast Sci.* **4** 0080
[21] Driver T, Mountney M, Wang J *et al.* 2024 *Nature* **632** 762
[22] Yun H, Mun J H, Hwang S I, Park S B, Ivanov I A, Nam C H, and Kim K T 2018 *Nat. Photon.* **12** 620
[23] Vigneau J N, Nguyen-Dang T T, Charron E, and Atabek O 2022 *J. Chem. Phys.* **157** 134304
[24] Fukahori S, Kubo A, and Hasegawa H 2024 *Phys. Chem. Chem. Phys.* **26** 26277
[25] Asghar H, Ali R, and Baig M A 2013 *Phys. Plasmas* **20** 123302
[26] Belmonte M T, Djurović S, Peláez R J, Aparicio J A, and Mar S 2014 *Mon. Not. R. Astron. Soc.* **445** 3345
[27] Zimmermann H, Buller J, Eilzer S, and Eichmann U 2015 *Phys. Rev. Lett.* **114** 123003
[28] Suzuki N, Kosugi S, Ito Y, Inoue N, Nagoshi T, Kuze N, Harries J R, Sullivan J P, Nagata T, Sokell E, Koike F, and Azuma Y 2016 *J. Phys. B: At. Mol. Opt. Phys.* **49** 145002
[29] Sukhorukov V L, Petrov I D, Schäfer M, Merkt F, Ruf M W, and Hotop H 2012 *J. Phys. B: At. Mol. Opt. Phys.* **45** 092001
[30] Chini M, Wang X W, Cheng Y, Wang H, Wu Y, Cunningham E, Li P C, Heslar J, Telnov D A, Chu S I, and Chang Z H 2014 *Nat. Photon.* **8** 437
[31] Bengtsson S, Larsen E W, Kroon D, Camp S, Miranda M, Arnold C L, L'Huillier A, Schafer K J, Gaarde M B, Rippe L, and Mauritsson J 2017 *Nat. Photon.* **11** 252
[32] Beaulieu S, Bloch E, Barreau L, Comby A, Descamps D, Géneaux R, Légaré F, Petit S, and Mairesse Y 2017 *Phys. Rev. A* **95** 041401
[33] Vujnović V and Wiese W L 1992 *J. Phys. Chem. Ref. Data* **21** 919
[34] Hibbert A and Hansen J E 1994 *J. Phys. B: At. Mol. Opt. Phys.* **27** 3325
[35] Whaling W, Anderson W H C, Carle M T, Brault J W, and Zarem H A 1995 *J. Quant. Spectrosc. Radiat. Transfer* **53** 22
[36] Aparicio J A, Gigosos M A, and Mar S 1997 *J. Phys. B: At. Mol. Opt. Phys.* **30** 3141
[37] Saloman E B 2010 *J. Phys. Chem. Ref. Data* **39** 033101
[38] Djurović S, Blagojević B, and Konjević N 2023 *J. Phys. Chem. Ref. Data* **52** 031503
[39] Kramida A, Ralchenko Y, Reader J, and NIST ASD Team 2024 *NIST Standard Reference Database* **5.12**